Journal of Materials Chemistry C

Ligand-Mediated Synthesis of Chemically Tailored Two-Dimensional All-Inorganic Perovskite Nanoplatelets Under Ambient Conditions

Journal:	*Journal of Materials Chemistry C*
Manuscript ID	TC-ART-06-2021-002931.R1
Article Type:	Paper
Date Submitted by the Author:	05-Sep-2021
Complete List of Authors:	Davis, Andrew; Syracuse University, Chemistry Li, Shuuya; SUNY-ESF, Chemistry Lin, Hanjie; Syracuse University, Chemistry Chu, Chun; Syracuse University, Chemistry Franck, John; Syracuse University, Chemistry Leem, Gyu; State University of New York College of Environmental Science and Forestry at Syracuse, Chemistry Maye, Mathew; Syracuse University, Department of Chemistry Zheng, Weiwei; Syracuse University, Chemistry

Ligand-Mediated Synthesis of Chemically Tailored Two-Dimensional All-Inorganic Perovskite Nanoplatelets Under Ambient Conditions

Received 00th January 20xx,
Accepted 00th January 20xx

DOI: 10.1039/x0xx00000x

Andrew H. Davis,[a] Shuya Li,[b] Hanjie Lin,[a] Chun Chu,[a] John M. Franck,[a] Gyu Leem,[b,c] Mathew M. Maye,[a] and Weiwei Zheng[†,a]

Abstract

All-inorganic halide perovskite nanocrystals (NCs) offer impressive optoelectronic properties for light harvesting, energy conversion, and photoredox applications, with two-dimensional (2D) perovskite NCs further increasing these prospects due to their improved photoluminescence (PL) tuneability, impressive color purity, high in-plane charge transport, and large lateral dimensions which is advantageous for device integration. However, the synthesis of 2D perovskites is still challenging, especially toward large-scale applications. In this study, through the control of surface ligand composition and concentration of a mixture of short (octanoic acid and octylamine, 8-carbon chain) and long (oleic acid and oleylamine, 18-carbon chain) ligands, we have developed an extremely facile ligand-mediated synthesis of 2D $CsPbX_3$ (X = Cl, Br, or mixture thereof) nanoplatelets (NPLs) at room temperature in an open vessel. In addition, the developed method is highly versatile and can be applied to synthesize Mn-doped $CsPbX_3$ NPLs, showing a systematic increase in the total PL quantum yield and the Mn-dopant emission around 600 nm with increasing Mn and Cl concentrations. The reaction occurs in toluene by the introduction of a CsX, PbX_2, and MnX_2 precursor under ambient conditions, which requires no harsh acids, avoids excessive lead waste, little thermal energy input, and is potentially scalable toward industrial applications.

Introduction

Semiconductor perovskite nanocrystals (NCs) have been of recent interest due to their impressive optical properties for optoelectronic applications. Of these NC systems, all-inorganic metal halide perovskite NCs offer increased thermal and moisture stability with excellent optoelectronic properties in comparison to hybrid organic-inorganic perovskite NCs.[1-6] Further shape control of all-inorganic perovskites has led to two-dimensional (2D) perovskite NCs, such as nanoplatelets (NPLs) and nanosheets (NSs),[7-15] that are of keen interest due to their extremely narrow absorption and emission spectra,[7, 9, 16-18] excellent in-plane charge transport,[18, 19] and large lateral sizes useful for device integration.[7, 15-19]

The continued development of perovskite-based devices and applications relies on the availability of dependable synthetic methods with controlled composition, size, and morphology.[20-24] Current syntheses for 2D all-inorganic halide perovskite NCs, with general ABX_3 structure, rely primarily on three distinct methods, including the template method by cation exchange of premade hybrid 2D perovskite NCs,[25] direct synthesis by manipulating experimental parameters including ligands, solvent, temperature, pressure, etc.,[15, 26-37] and the assembly method involving the fabrication of 2D NCs from 1D nanorods[15, 38] or larger 2D NSs from the laterally smaller 2D NPLs.[15, 39] In the template and assembly methods, either well-established hybrid perovskite synthetic techniques must be utilized or 1D NCs must be first synthesized prior to the desired 2D NC formation. This adds to the cost and complexity of the synthesis, making it strenuous for further sample preparation toward device integration. Therefore, direct synthetic control through temperature, pressure, and surface ligand manipulation is highly desired as it provides an avenue for facile and cost-effective syntheses with the potential to be scaled for practical applications.[40]

Recent reports have shown that 2D $CsPbBr_3$ perovskite NCs are capable of being directly synthesized under ambient conditions.[41-46] These room-temperature syntheses for 2D NPLs typically involve the use of excess lead salts dissolved in aprotic polar solvents and HBr. Excess lead forces the resulting structure toward the formation of the $CsPb_2X_5$, often associated with 2D NCs, while HBr protonates amine ligands causing competitive binding environments during vertical growth and has thus been used rather successfully to control NC thickness.[37, 47, 48] Multiple of these syntheses also use high temperatures during Cs-oleate precursor preparation even though the final reactions between PbX_2 and Cs-oleate occurred at room temperature.[43-45, 49] This is owing to the low solubility of CsX in the desired polar aprotic solvent and have thus limited the applicability and versatility of these room temperature reactions for 2D NC growth. The aforementioned syntheses are, therefore, hindered by their use of strong acids, excessively high lead concentrations, high temperature precursor syntheses, or limited synthetic versatility despite their availability.

[a] *Department of Chemistry, Syracuse University, Syracuse, New York 13244, United States.*
[b] *Department of Chemistry, State University of New York College of Environmental Science and Forestry, Syracuse, NY 13210, United States.*
[c] *The Michael M. Szwarc Polymer Research Institute, Syracuse, New York 13210, United States.*
† **Corresponding Author**: Weiwei Zheng
ORCID: Weiwei Zheng: 0000-0003-1394-1806
Email: Wzehn104@syr.edu
Electronic Supplementary Information (ESI) available: [All characterization data (optical spectra, TEM, and AFM) for control experiments of ligand composition and precursor injection time (PDF)]. See DOI: 10.1039/x0xx00000x

The use of strong acid in perovskite NC synthesis should be minimized as it can cause NC degradation, even though NCs will often boast increased PLQYs immediately following synthesis. Additionally, while large molar concentrations of lead have been shown to promote 2D NC growth,[42, 45] this should be approached with caution and concern as excess lead waste should be avoided whenever possible. Synthetic routes that utilize Cs-oleate precursors require large thermal energy input, under controlled conditions for proper preparation, limiting the utility of the subsequent ambient synthesis.[43] Finally, despite the successful formation of 2D $CsPbBr_3$ NCs by the HBr-assisted growth method, other 2D halide perovskite NCs can only be obtained by anion exchange. The direct growth of 2D $CsPbCl_3$ and $CsPbI_3$ perovskite NCs has not yet been realized by these methods. Therefore, the direct growth of 2D $CsPbX_3$ NCs under green and ambient conditions is still challenging.

Surface-bound organic ligands are typically used to passivate the surface traps of colloidal NCs, which also modulates the surface energy of the NCs by introducing different surfactants/ligands that adsorb onto growing surfaces. When surfactants stabilize a certain surface by "selective adhesion," the surface energy and growth rate can vary between different crystallographic directions.[15, 36, 50] Deng *et al.* theorized that ligand composition assisted the formation of varying NC morphologies through solubility interactions as the ligands and metal precursors in polar aprotic solvent were introduced into a poor solvent like toluene. Therefore, NC formation is initiated by reprecipitation of the dissolved metal ion salts, where reverse micelles form as a contrast between the polar aprotic solvent and the nonpolar toluene, resulting in rapid NC formation. The resulting NC growth would be highly dependent on the hydrophobic and electrostatic interactions of the metal ions and the introduced ligands within the two solvent systems. For example, acetic acid and dodecylamine were introduced to cause quantum dot formation, while oleic acid and octylamine caused nanoplatelet formation.[43] Therefore, modulating the ligand composition can have a massive effect on the resulting NC morphology. In fact, Pan *et al.*, devised a ligand and temperature mediated method for the discrete control of NC thickness, synthesizing 0D and 2D $CsPbBr_3$ NCs carboxylic acid and mine ligands of varying hydrocarbon chain lengths at elevated temperature of 140 to 170 °C.[51] The soft ionic nature of inorganic lead halide perovskite NCs supports ligand mediated methods as it is highly susceptible to delicate changes in the surface chemical environment.[52]

In this study, we design a rigorous ligand-mediated room temperature synthesis for the direct fabrication of 2D quantum confined $CsPbX_3$ and Mn-doped $CsPbX_3$ (X = Cl, Br, and mixture thereof) NPLs without the use of strong acids, high Pb concentration, or high temperature for precursor preparation or NC growth. This facile reaction uses the direct control of ligand composition in combination with polar aprotic N,N-dimethyl formamide (DMF) and dimethyl sulfoxide (DMSO) solvents to dissolve Cs, Pb, and Mn-precursors, which are then introduced into toluene, causing near instantaneous 2D NC formation. Direct NC size and morphological control has been implemented by controlling the ligand concentration and composition, with the chosen oleic acid (OA), oleylamine (OAm), octanoic acid (OctAc), and octylamine (OctAm) ligands providing a near perfect environment for the development of anisotropic 2D NCs. The resulting reaction is extremely facile, highly reproducible and easily manipulated ~~by both scale and~~ composition with ease, resulting in a synthetically versatile reaction that can be modified for the direct synthesis of Mn:$CsPbX_3$ (X = Cl, Br, and mixture thereof) NCs of varying Mn doping concentration without the use of anion exchange. The resulting facile, cost-effective, and potentially scalable reaction is promising for larger scale synthesis of 2D perovskite NCs for industry applications.

Results and Discussion

Optimized ligand composition and concentration. In this work, we employed the use of two separate size categories of ligands (both acid and base) to directly synthesize 2D $CsPbCl_3$, $CsPbBr_3$, and $CsPbCl_{3-x}Br_x$ NCs and their Mn-doped equivalents entirely under ambient conditions. Specifically, OA and OAm 18-carbon chain ligands as well as OctAc and OctAm 8-carbon chain ligands were employed to strategically tune the surface energy of the growing NC planes. The ligand environment was carefully selected by a progression of control experiments that started with ligand concentration and compositional studies for OA and OAm long ligands (Figure S1 and S2) and progressed to the introduction of OctAc and OctAm short ligands (Figure S3 and S4). This method involves no additional dehydration or degassing steps for solvents or precursors, except for the storage of CsX, PbX_2, and MnX_2 in a moisture-free inert atmosphere due to their hygroscopic nature.

Control experiments initially focused on the composition of OA/OAm long ligands for $CsPbBr_3$ NC synthesis without the presence of short ligands. Results showed that long ligand compositions of 20% - 40% [OAm] are viable options for 2D or quasi-2D NC formation at a total ligand concentration of 150 µL, however, 20% was chosen as it provided a similarly blue shifted emissions with relatively high PLQY and narrow FWHM (Figure S1), while also presenting high quality monodisperse NCs via TEM analysis (Figure S2). Additionally, it was determined that higher and lower total ligand concentrations resulted in decreased NC monodispersity.

Table 1. Summarized volumetric ligand composition statistics and optical analysis for the synthesis of 2D $CsPbBr_3$ NPLs.

Ligand Composition (%Vol)				Results				
Long Ligands		Short Ligands		$\lambda_{host\ PL}$	FWHM	Thickness	PLQY	Lifetime
OA	OAm	OctAc	OctAm	(nm)	(nm)	(nm)	(%)	(ns)
80%	20%	0%	0%	512	13	~7.4	31%	66
64%	16%	15%	5%	498	11	~4.8	49%	45

Manna *et al.*[36] and Zheng *et al.*[15] previously reported that low concentrations of short ligands assist in the synthesis of anisotropic NCs under high temperature and pressure conditions. Our results indicate that short ligands play an important role in anisotropic growth at room temperature, even though the ligand solution should consist primarily of

longer ligands for proper NC growth. A short ligand concentration of 20% with a composition of 75% [OctAc] to 25% [OctAm] (Figure S3) was selected because it provides consistently strong (PLQY ~40%), blue shifted (from 512 to ~498 nm) emissions with narrow FWHM (~11 – 13 nm), as well as short PL lifetime (<50 ns) for $CsPbBr_3$ NCs, which is consistent with 2D NC formation. From the blue-shifted PL position, we can estimate 7-8 monolayers thickness of the 2D $CsPbBr_3$ NPLs, ~4-5 nm, based on the quantum confinement effect.[37, 53, 54] Atomic force microscopy (AFM) analysis confirms that the introduction of short ligands into a $CsPbBr_3$ NC system results in a significant decrease in thickness from ~7.4 to 4.8 nm (Figure S4).

For proper 2D NC formation, the ideal total ligand composition was determined to be 80% long ligand and 20% short ligand at a ratio of 75-80% acids to 20-25% amine ligands, summarized in Table 1. Results from $CsPbBr_3$ studies were also shown to translate to $CsPbCl_3$ and mixed halide NCs with a substantial narrowing of the emission FWHM resulting with increasing [Cl^-] anion concentration. In addition, the NC growth behavior was simultaneously tested with precursor injection times into the toluene solution (Figure S5 and S6). It was determined that, while fast injections could produce desired results, 1 min injection time produced more consistent NCs, while injection times exceeding 1 min reduced monodispersity of the NC system. These conditions were chosen as they produced consistent results for the desired composition and were held consistent during Mn introduction.

Direct synthesis of 2D all-inorganic metal halide perovskite NCs. Halide compositional control was introduced with slightly differing synthetic parameters for the direct synthesis of $CsPbBr_3$, $CsPbCl_3$, and mixed halide systems. In our method, ligand concentrations and ratios were maintained throughout all halide compositions, however, solvent systems had to be varied for each composition as $CsPbBr_3$ preferred DMF as its primary solvent and $CsPbCl_3$ preferred DMSO as its primary solvent. Mixed halide composition NC syntheses required proportional solvent concentrations to their halide compositions.

The results of the halide compositional study of 2D $CsPbCl_{3-x}Br_x$ NPLs are summarized in Figure 1. Transmission electron microscopy (TEM) images indicate a 2D morphology with lateral dimensions measuring 16 ± 3 nm, 15 ± 3 nm, and 18 ± 3 nm for $CsPbBr_3$, $CsPbCl_2Br$, and $CsPbCl_3$ NPLs, respectively (Figure 1a-1c). The complete set of undoped TEM images can be found in Figure S7 of the SI. High-resolution TEM images show lattice structures along the (110) lattice plane, indicating an increase in d-spacing with bromide concentration ([Br]) (0.42 nm for $CsPbCl_3$, 0.43 nm for $CsPbCl_2Br$, and 0.45 nm for $CsPbBr_3$), which is in good agreement with theoretical d-spacing values of 0.40 and 0.42 for $CsPbCl_3$ and $CsPbBr_3$, respectively, as well as their increased lattice parameters with the incorporation of larger Br anions. From the optical data presented in Figure 1d, a clear PL peak red-shift from 408 to 501 nm is observed with [Br] of 0% to 100%, respectively, due to the decrease in bandgap from $CsPbCl_3$ to $CsPbBr_3$ (Figure 1e). Furthermore, extremely narrow PL FWHM, from 7.5 to 14.0 nm for [Br] of 0% and 100%, respectively, was observed for the samples, which indicates high monodispersity and the uniform thickness of the 2D NPLs (Figure 1f). The increased PL FWHM from Cl rich to Br rich perovskite NPLs is expected as $CsPbCl_3$ notably has an extremely narrow host emission with $CsPbBr_3$ often producing a stronger PLQY yet with a slightly broader emission. Notably, the PLQY did in fact increase with [Br] from 5% with $CsPbCl_3$ to 49% with $CsPbBr_3$ (Figure 1g).

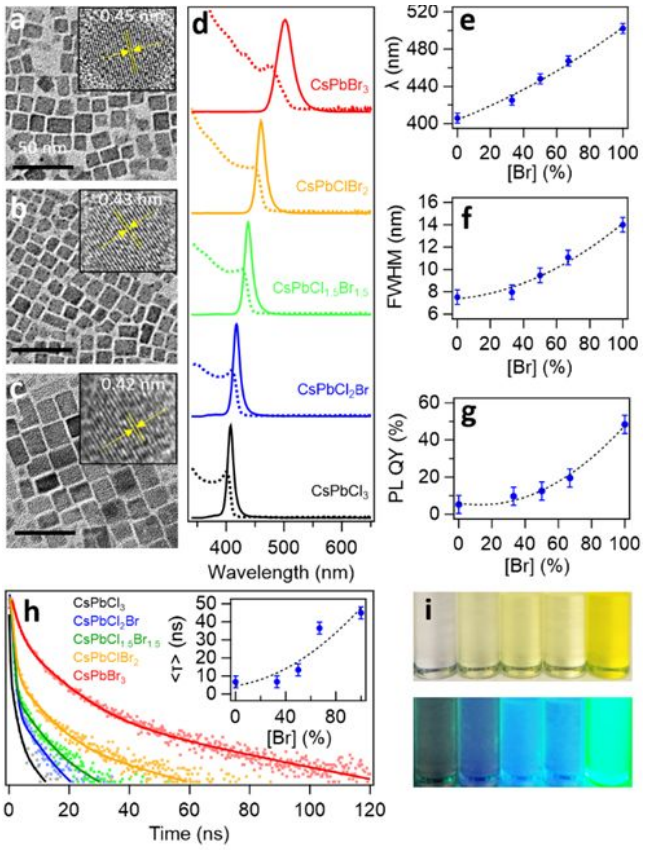

Figure 1. Undoped $CsPbX_3$ (X = Cl, Br, and mixture thereof) NPLs varying in [Br] from 0% to 100%. Representative TEM images scaling respectively, from the top to bottom, as (a) $CsPbBr_3$, (b) $CsPbCl_2Br$, and (c) $CsPbCl_3$ NPLs, with the insets being respective high-resolution TEM images showing d-spacing of the (110) lattice plane. (d) Representative absorbance (dashed line) and PL data for [Br] = 0%, 33%, 50%, 67%, and 100%. (e – g) Averaged optical analysis values for (e) host PL peak position and (f) host PL FWHM, and (g) total PLQY for each of the respective PL emissions of varying [Br], generated from the analysis of 10 separate syntheses. (h) Representative time-dependent PL spectra with the resulting average lifetime decay (inset) for $CsPbX_3$ NCs, where X = (Cl, Br and a mixture thereof). (i) Images of $CsPbX_3$ (X = Cl, Br, and mixture thereof) NPLs in toluene solution under ambient light (top) and 365 nm UV light irradiation (bottom).

Time-dependent PL measurements show an increase in PL lifetime decay from ~7 ns ($CsPbCl_3$) to ~45 ns ($CsPbBr_3$) with increasing [Br] (Figure 1h). These results are consistent with an increase in PLQY, which often results in longer lifetime decays. The optical shift with [Br] can be directly observed in Figure 1i from left to right resulting in a red-shifted emission where the NC solutions are imaged under ambient light (top) and 365 nm UV irradiation (bottom). It should be noted that $CsPbI_3$ NCs were attempted using a similar method yet resulted in structurally unstable products that decomposed to the optically

inactive orthorhombic phase prior to obtaining optical spectra (within ~1 min). It is likely that stable $CsPbI_3$ NCs cannot be soundly synthesized under these current synthetic conditions without proper solvent purification and an inert atmosphere, which is outside the reach and desired interests of this study.

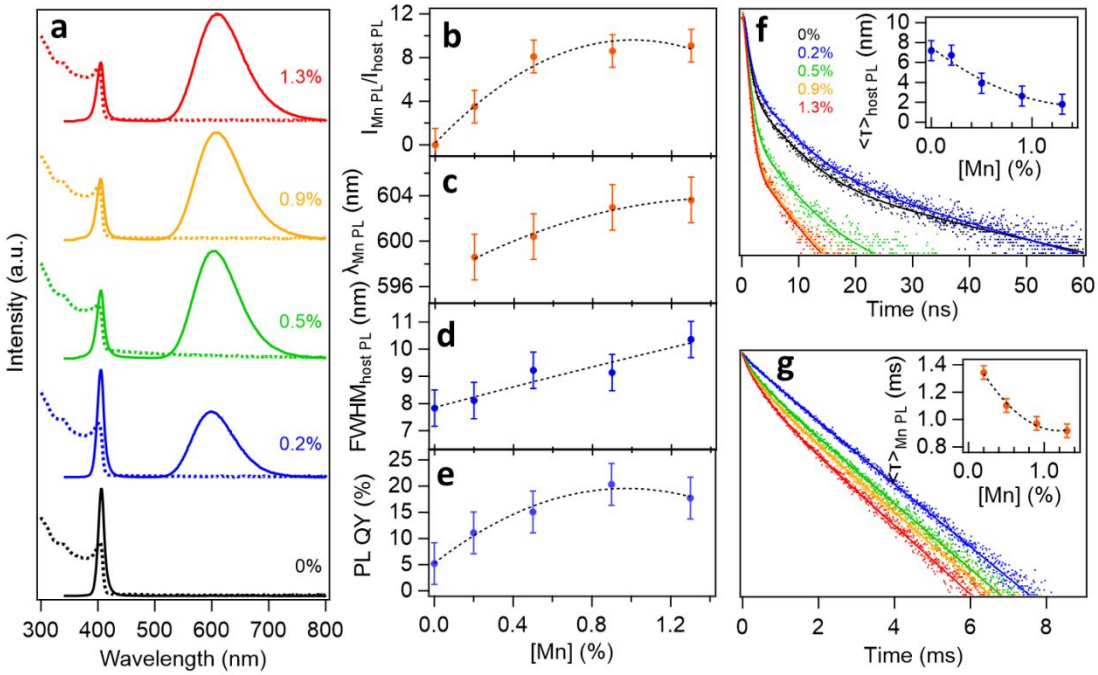

Figure 2. Manganese concentration dependent optical properties of doped $CsPbCl_3$ NPLs from 0% to 1.3% [Mn]. (a) Absorption (dashed lines) and PL (solid lines) spectra with corresponding spectral analysis by (b) Mn-to-host PL peak ratio based on the integrated peak area. (c) Mn PL peak position, (d) host PL FWHM, and (e) total spectral PLQY. Time dependent PL for (f) host PL and (g) Mn PL (inset: average PL lifetime Decay for the given samples with respect to [Mn]). Error was calculated as the standard deviation of a population of 10 repeated samples for each sample.

Direct synthesis of Mn-doped 2D $CsPbCl_3$ perovskite NCs. Further synthetic control was introduced by Mn-doping in both $CsPbCl_3$ (Figure 2 and Figure 3, TEM in Figure 4c and Figure S9) and mixed halide $CsPbCl_{3-x}Br_x$ NCs to explore the versatility of the ligand-mediated 2D NC growth at room temperature (Figure 4). Mn(II) was chosen as the most prominent dopant in perovskites to date, and as a possible dopant capable of orange emission in high [Br] systems, as well as the potential to increase NC stability and PLQY. However, dopant incorporation in perovskite NCs has proven difficult due to the large cation size mismatch between Pb^{2+} (119 pm) and common transition metal dopant ions, such as Mn^{2+} (83 pm), leading to relatively low dopant ion incorporation in the NC lattice even with high dopant ion concentrations in solution.[55-57]

For Mn doped 2D $CsPbCl_3$ NPLs, increased Mn PL was observed with dopant introduction concentrations (Figure 2a, Figure S8), which indicates Mn dopant incorporation inside the $CsPbCl_3$ perovskite lattice and efficient host NC to Mn dopant energy transfer. Upon the introduction of 0% to 300% Mn:Pb molar concentration $MnCl_2$ into the reaction system, 0% to 1.3% Mn dopant incorporation resulted, as determined by elemental analysis using inductively coupled plasma optical emission spectroscopy (ICP-OES).

Figure 2b shows that the Mn-to-host peak intensity ratio continually increases from 0 at 0% manganese concentration ([Mn]) to 9.1 at 1.3% [Mn]. The FWHM of the host PL spectra are extremely narrow, increasing from 7.8 and 10.4 nm with [Mn] (Figure 2d). Further investigation of the optical spectra shows a distinct red-shift of the Mn PL which shifts from 598 to 604 nm from 0.2% to 1.3% [Mn] (Figure 2c), as well as an increased FWHM of the Mn emission from 86 to 95 nm. This indicates that the bonding environment of Mn is changing with increased [Mn], likely with broader substitutional sites as more dopants are incorporated inside the NPL lattice. The dopant depth-dependent Mn emission red-shift, due to the shell applied pressure on dopants, has been observed in Mn doped CdS/ZnS core/shell NCs previously.[58-63] It is also possible to have similar pressure behavior caused by internal lattice strain, causing a spring like torsion or compression effect on the dopant sites, causing distortion of the Mn-coordination.[63] Interestingly, the total PLQY of the resulting NCs increases drastically with the introduction of Mn, from 5% at 0% Mn to a maximum of 21% at 0.9% Mn due to the prevalence of the Mn emission peak at around ~600 nm with increasing [Mn] (Figure 2e). The PLQY slightly decreases following 0.9% Mn introduction from 21% to 18% PLQY at 1.3% [Mn], which is likely due to the concentration quenching effect that occurs at higher Mn doping concentrations, as previously observed in doped NCs.[61, 62, 64]

Figure 2f shows that the host PL lifetime decay drastically changes with the introduction of Mn as the average lifetime decay (Figure 2f, inset) decreases from 7.2 to 1.8 ns at 0% and 1.3% [Mn], respectively. This effect occurs due to increased efficient host to Mn dopants energy transfer and an increase in available Mn-decay pathways with increasing [Mn]. Additionally, the continual decrease in the average Mn PL lifetime, from 1.3 to 0.9 ms at 0.2 and 1.3% [Mn], respectively

(Figure 2g and inset), further supports the Mn concentration quenching effect, as short-ranged Mn-Mn interactions occur causing a reduced PL lifetime.[61]

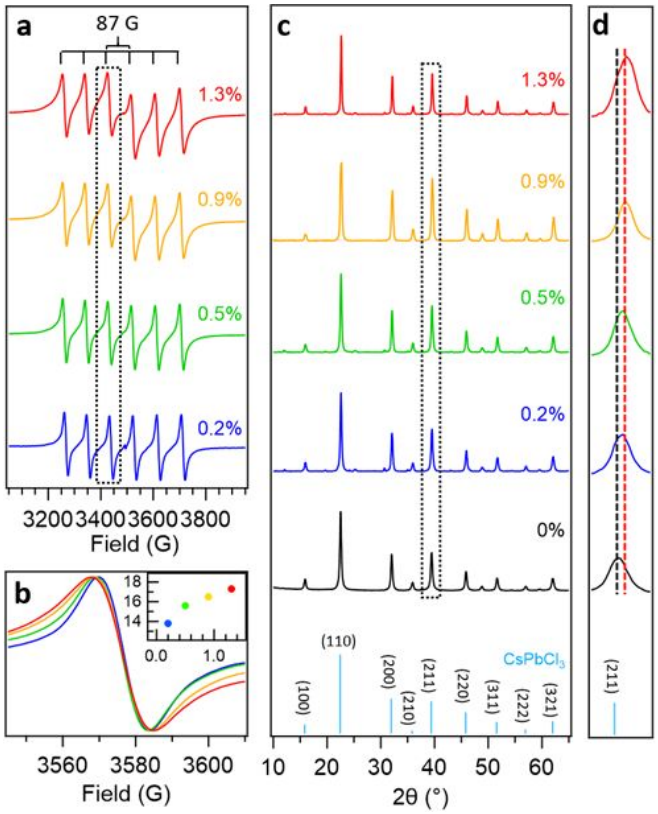

Figure 3. (a) X-band EPR spectra for Mn-doped $CsPbCl_3$ NPLs, (b) the representative 3rd sextet hyperfine peak of Mn:$CsPbCl_3$ NPL EPR spectra to display increasing spectral linewidth with increasing [Mn], inset shows the EPR spectral linewidth. (c) XRD for Mn-doped $CsPbCl_3$ NPLs of varying [Mn] from 0% to 1.3%. (d) Zoomed-in XRD patterns showing peak shifting of the (211) diffraction peak by increasing the Mn-doping concentration.

Further investigation of the Mn-doped $CsPbCl_3$ NCs was performed through room temperature X-band electron paramagnetic resonance (EPR) spectroscopy and powder X-ray diffraction (XRD). EPR showed that Mn was largely introduced in the NC core, with a sextet hyperfine splitting pattern of A = 87 G (Figure 3a) being similar to the 86 G splitting constant observed in other Mn core doped perovskite systems.[62, 64, 65] The average linewidth of the hyperfine splitting increased from 13.8 to 17.3 G with [Mn] from 0.2% to 1.3% indicating broader/different Mn bonding environments in the samples with higher [Mn] (Figure 3b and inset).[66] Additionally, a broad dipolar background is observed in the 1.3% [Mn] sample indicative of Mn-Mn short-range interactions, which is consistent with higher Mn doping concentration for 2D NPLs. XRD pattern of the doped NPLs are consistent with cubic phase $CsPbCl_3$ NCs (Figure 3c). With dopant incorporation, a slight increase in the diffraction angle can be observed that increases with [Mn]. For example, the XRD peak associated with the (211) lattice plane shifts 0.06°, 0.08°, 0.13°, and 0.14° for 0.2%, 0.5%, 0.9%, and 1.3% [Mn] samples, respectively. This shift in lattice structure is consistent with lattice contraction with the incorporation of the much smaller Mn^{2+} ions in place of Pb^{2+}.

Direct synthesis of Mn-doped 2D CsPbX3 (X = Cl, Br, and mixture thereof) perovskite NCs. Mn doping was further tested in mixed halide systems to observe the Mn PL and structural properties with halide composition. These mixed halide NPLs were directly synthesized by carefully matching $MnBr_2$ and $MnCl_2$ concentrations with proportional concentrations of DMF and DMSO to the [Br] at 100% Mn:Pb molar concentration. TEM images (Figure 4a to 4c) show that dopant incorporation did not largely affect the growth behavior of the 2D NCs, still resulting in nearly square-shaped NPLs of 15 ± 3 nm, 17 ± 6 nm, and 18 ± 4 nm in average lateral length for Mn-doped $CsPbBr_3$ (Figure 4a), $CsPbCl_{1.5}Br_{1.5}$ (Figure 4b), and $CsPbCl_3$ (Figure 4c), respectively. The complete set of TEM images for Mn:$CsPbCl_2Br$ NPLs with varying Mn-dopant molar concentration (0.2% - 1.2%) have been provided in the SI as Figure S10. However, a slight decrease in the d-spacing can be observed in the high-resolution TEM (insets in Figure 4a–4c) compared with undoped NPL count parts, likely due to lattice compression after Mn doping. The XRD peaks continuously shifts to lower angles from undoped $CsPbCl_3$ to $CsPbBr_3$, which is consistent with the formation of mixed halide compositions approaching pure $CsPbBr_3$. In addition, the lattice compression after doping is further observed from the XRD of the Mn-doped (top) and undoped (bottom) $CsPbX_3$ NCs (Figure 4d). For example, the XRD peak at ~39° associated with the (211) lattice plane shifts by ~0.1° for Mn-doped NPLs, with respect to their undoped counterparts (Figure 4e).

Despite the consistent maintenance of 100% Mn:Pb mol% synthetic dopant concentration throughout these Mn-doped samples, ICP-OES elemental analysis of shows that [Mn] generally increases from 0.5% to 2.9% from 0% to 100% [Br], where Mn:$CsPbCl_3$, Mn:$CsPbCl_2Br$, Mn:$CsPbCl_{1.5}Br_{1.5}$, Mn:$CsPbClBr_2$, and Mn:$CsPbBr_3$ were doped with 0.5%, 0.5%, 0.9%, 1.8%, and 2.9% [Mn], respectively. X-band EPR analysis (Figure 4f) shows increased dipolar contribution, from increasing Mn-Mn coupling with increased [Br], which is consistent with the higher [Mn] for Br rich NPLs from ICP-OES results.

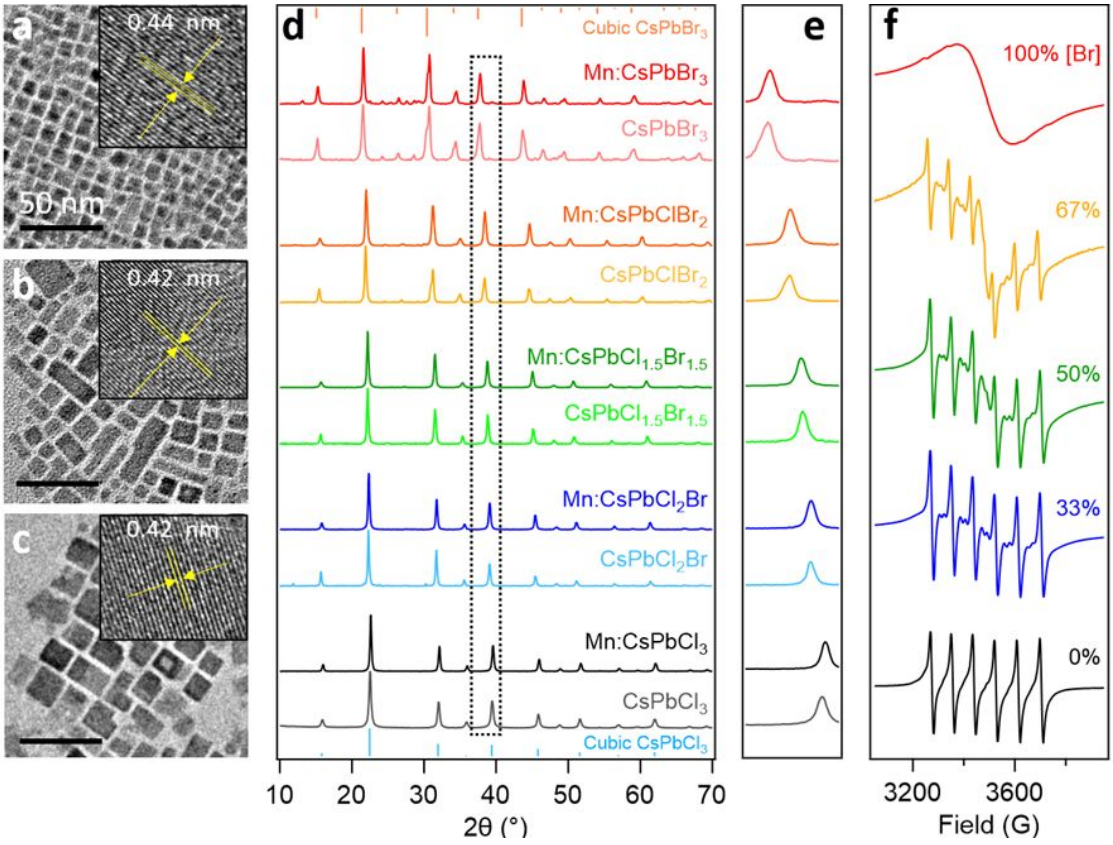

Figure 4. TEM images of (a) Mn:$CsPbBr_3$, (b) Mn:$CsPbCl_{1.5}Br_{1.5}$, and (c) Mn:$CsPbCl_3$ NPLs, (d) XRD of Mn-doped and undoped $CsPbX_3$ (X = Cl, Br, and mixture thereof) NPLs, (e) Zoomed-in XRD patterns showing peak shifting of the (211) diffraction peak by Mn dopant incorporation, and (f) EPR spectra for $CsPbX_3$ NPLs of varying [Br] ranging from 0% to 100% halide composition.

Figure 5a shows an optical spectral comparison on Mn-doped and undoped $CsPbX_3$ NPLs, where ~4 nm PL blue-shifts can be observed in Figure 5a and 5c for these 2D $CsPbCl_{3-x}Br_x$ NPLs, which is due to lattice compression with the introduction of smaller Mn^{2+} ions in place of the larger Pb^{2+} ions. Additionally, a strong Mn PL is observed in Cl^- rich samples, however, a decrease in the Mn-to-host PL area ratio decreases from 7.4 to 0 for Mn:$CsPbCl_3$ to Mn:$CsPbBr_3$, respectively (Figure 5a and 5d). Given that the $CsPbBr_3$ bandgap is large enough to encompass the $^4T_1$ and $^6A_1$ Mn energy levels, a Mn PL from an host-to-dopant energy transfer could be observed, however, the Mn PL is absent in the Mn:$CsPbBr_3$ NPLs (Figure 5a). This phenomenon has been observed in similar Mn:$CsPbBr_3$ NC systems and has recently been proposed to be driven by a back energy transfer mechanism where the $^4T_1$ Mn atomic band is so close to the conduction band of $CsPbBr_3$ that the energy transfer to Mn is repurposed back to the host conduction band by a thermally driven pathway, decreasing the Mn PL (Figure 5b).[67]

Significantly, an increase in PLQY is also observed with dopant introduction (Figure 5e). For Cl rich NPLs this effect can be easily explained due to the appearance of the Mn emission spectra at ~600 nm, however, due the constricting of the host bandgap as [Br] increases, Mn peak intensity decreases at higher [Br] and quenched in $CsPbBr_3$ NPLs (Figure 5a). Therefore, the increasing PLQY must also be caused by at least one additional factor, which we speculate is an overall increase in structural stability according to the Goldschmidt tolerance factor ($t = \frac{r_A + r_x}{\sqrt{2}(r_B + r_x)}$). With the introduction of the smaller Mn^{2+} ions, where r is equal to the ionic radii of the respective ions in the ABX_3 perovskite structure, the tolerance factor should increase.[68] Consequently, with the stability range for this tolerance factor being between ~0.825 and 1.059, the desired value for the tolerance factor should be a more central value around ~0.942 as structural stability drastically decreases closer to the edge of the tolerance factor range.[40] Therefore, a decrease in the average radius of the B-site ion would result in an increase in the tolerance factor for a more stable structure, according to the respective tolerance factors of $CsPbCl_3$ and $CsPbBr_3$ being 0.914 and 0.907. Indeed, the introduction of Mn^{2+} increases the tolerance factor closer to 0.942 causing an increase in structural stability of the [Br] rich samples and a resulting increase in exciton recombination energy that then increases the host bandgap PLQY without the introduction of a Mn PL.

Time-dependent PL spectra (Figure 5f and 5g) are consistent with the introduction of dopant ions, where the average host PL lifetime significantly decreases upon Mn-dopant introduction and increases from 2.8 to 21.6 ns with increasing [Br] from 0% to 100%, respectively (inset in Figure 5f). This effect likely occurs due to the increased PLQY of the higher [Br] samples. Figure 5g shows that the Mn lifetime decay decreases with [Br] from 1.2

to 0.5 ms, indicating that the structures are likely experiencing increased Mn-Mn short-ranged interactions and Mn concentration quenching effects due to the higher [Mn] in Br rich NPLs.[64]

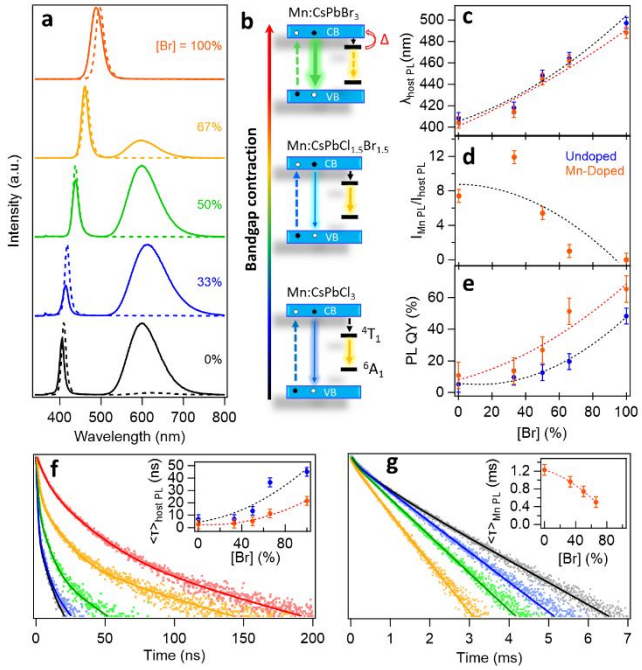

Figure 5. (a) Optical spectra comparison between undoped (dashed line) and Mn-doped (solid line) $CsPbX_3$ (X = Cl, Br, and mixture thereof) NPLs. (b) schematic representation of the host and Mn band-alignment with dopant incorporation for Mn:$CsPbBr_3$ (top), Mn:$CsPbCl_{1.5}Br_{1.5}$ (middle), and Mn:$CsPbCl_3$ (bottom). (c-e) Spectral analysis data for (c) host PL peak position, (d) Mn-to-host PL ratio based on the integrated peak area, and (e) total PLQY. Lifetime decay of the (f) host PL and (g) Mn PL of Mn-doped NPLs, with respect to [Br]. The inset in (f) presents a comparison of the average host PL lifetime between the undoped and Mn-doped NPLs, whereas the inset in (g) represents the average Mn PL lifetime.

Conclusions

We have developed a facile ligand-mediated synthetic method for the structural and morphological engineering of 2D all-inorganic perovskite NPLs by the dropwise introduction of CsX and PbX_2 precursors into an open and rapidly stirring vial of toluene at room temperature. The resulting 2D NPLs have narrow FWHM, relatively high PLQYs, and short host PL lifetime decays. Furthermore, we were able to utilize this direct synthetic method for Mn-dopant incorporation, through the simple introduction of dopant ions into a Cs-Pb precursor prior to the NPL synthesis. The developed ligand-mediated synthetic method for 2D perovskite NPLs requires little energy input and no further precursor purification, while avoiding harsh conditions and excessive Pb concentrations, making it a promising synthetic route for the introduction of 2D perovskite NCs to industrial applications for further use in optoelectronics.

Experimental

Chemicals. Cesium bromide (CsBr, 99.999%, Alfa Aesar), cesium chloride (CsCl, 99.999%, Alfa Aesar), lead bromide ($PbBr_2$, 99.999% trace metal, Alfa Aesar), lead chloride ($PbCl_2$, 99.999% trace metal, Alfa Aesar), manganese bromide ($MnBr_2$, 99.9%, Alfa Aesar), manganese chloride ($MnCl_2$, 99.9%, Alfa Aesar), toluene (99.6%, LabChem), acetone (99.5%, Fisher), N,N-dimethylformamide (DMF, 99.9%, Fisher), Dimethylsulfoxide (DMSO, 99.9% Fisher), oleic acid (OA, 90%, Alfa Aesar), octanoic acid (OctAc, 98+%, Alfa Aesar), oleylamine (OAm, 70%, Sigma-Aldrich), 1-octylamine (OctAm, 99%, Alfa Aesar) were purchased and used without further purification.

Control experiments on ligand composition and concentration. Ligand composition and concentration experiments were conducted by varying the ligand volume introduced into the 15 mL centrifuge tube prior to Cs, Pb, and Mn introduction and sonication. This allowed for a simple method for ligand control where a single large Mn-Cs-Pb precursor could be prepared and tested in multiple ligand systems separated into their own 15 mL centrifuge tubes. Care was taken to ensure that total volumetric ligand concentration was maintained at 150 µL. Additionally, concentration reactions involved maintaining individual ligand composition ratios by increasing or decreasing each ligand proportionally for the desired volume. For example, the standard ligand concentration ratios used are 64% OA, 16% OAm, 15% OctAc, and 5% OctAm, therefore for a volumetric concentration of 150 µL, the individual ligand volumes would be 96 µL OA, 24 µL OAm, 22.5 µL OctAc, and 7.5 µL OctAm.

Preparation of Cs-Pb precursor and Mn-Cs-Pb precursor. For a standard 10 mL reaction, a 1 mL precursor consisting of 0.08 mmol PbX_2, 0.04 mmol CsX (X = Cl, Br, or mixture thereof), and DMF (for $CsPbBr_3$ synthesis), DMSO (for $CsPbCl_3$ synthesis), or mixture thereof ($CsPbCl_{3-x}Br_x$) is prepared in a glass vial by stirring vigorously until either entirely dissolved or dispersed. The precursor is then transferred to a 15 mL centrifuge tube containing the mixture of ligands and sonicated. Sonication using a VWR Ultrasonic bath (60 Hz), with room-temperature water, was implemented to fully disperse or dissolve precursor materials, which typically occurred within ~3-5 min. However, it should be noted that vigorous stirring can utilized interchangeably with sonication, albeit, often requiring significantly more time (~1 hr) rather than the relatively short time required for sonication.

A separate precursor is utilized for Mn-doping, where the $MnCl_2$ and $MnBr_2$ are dissolved in DMSO and DMF, respectively, at a 0.8 M concentration. A controlled volume of the resulting dopant precursor is then introduced into the Cs-Pb precursor mixture prior to sonication, at a ratio consistent with the halide composition for the reaction. Varying [Mn] is simplified by introduction of a known volume dopant precursor corresponding to the desired [Mn]. For example, a 100% [Mn] reaction of Mn:$CsPbCl_2Br$ NCs would consist of 0.54 mmol $PbCl_2$, 0.26 mmol $PbBr_2$, 0.27 mmol CsCl, 0.13 mmol CsBr, 0.54 mmol $MnCl_2$, 0.26 mmol $MnBr_2$, in 0.67 mL DMSO, and 0.33 mL DMF, requiring 1 mL Cs-Pb precursor, 67 µL $MnCl_2$ precursor, and 33 µL $MnBr_2$ precursor. This precursor can be easily scaled for more than one synthesis or for varying synthetic volumes.

Synthesis of 2D $CsPbX_3$ (X = Cl, Br, and mixture thereof) NCs. For the general synthesis, 1 mL of the Cs-Pb precursor is injected dropwise into 10 mL toluene, stirring vigorously, in a 50 mL centrifuge tube over the span of 1 min where it is allowed to react for an additional 5 min. The turbid solution is directly centrifuged at 5000 rpm for 5 min, where the clear supernatant solution is transferred to a separate 50 mL centrifuge tube and the precipitate containing unreacted precursors is discarded. The NC samples in supernatant solution is then cleaned by acetone introduction (until solution becomes turbid), centrifugation at 5000 rpm for 5 min, and dispersion in toluene before optical measurements. For TEM or AFM measurements, samples were instead dispersed in hexane before being drop-cast onto their respective grids. It should be noted that further cleaning can greatly affects NC colloidal stability as a lack of protective surface ligands will allow for large scale surface-to-surface interactions causing NC aggregation. For XRD, EPR, and ICP-OES measurements, the NCs are cleaned an additional 3 times using a combination of hexane as the solvent and acetone as the counter-solvent, and centrifugation to obtain the desired precipitate, which is then dried under vacuum until a fine powder is obtained.

Synthesis of 2D Mn:$CsPbX_3$ (X = Cl, Br, and mixture thereof) NCs. For Mn introduction, the same procedure is followed with the exception that the 0.8 M MnX_2 precursors, consistent with the halide composition and desired dopant concentration, are added into the Cs-Pb precursor as shown above. This precursor was then sonicated until fully dissolved. After dissolution, the dopant precursor was introduced into the ligand containing solution with the Cs-Pb precursor prior to sonication. The samples were sonicated until fully dissolved or distributed and then injected as described above. The same sample purification methods were used as 2D $CsPbX_3$ (X = Cl, Br, and mixture thereof) NCs.

Sample characterization. The morphology and size distribution of NCs were analyzed by TEM using a JEM 2100F (operated at an accelerating voltage of 200 kV). Powder XRD patterns were taken on a Bruker D2 Phaser with a LYKXEYE 1-dimensional silicon strip detector using Cu Kα radiation (λ =1.5406 Å). ICP-OES analysis was performed on a PerkinElmer Optima 3300DV. Room temperature X-band EPR spectra were recorded at a microwave frequency of 9.4 GHz on a Bruker ELEXSYS-II E500 spectrometer. Absorption spectra were collected using an Agilent Cary 60 spectrophotometer. The PL measurements were conducted with a Horiba FluoroMax Plus spectrofluorometer. Time-resolved emission measurements were conducted using the time correlate single photon counting (TCSPC) for host PL and a μF2 60 W xenon flashlamp for Mn PL on an Edinburgh FLS-980. Tapping phase AFM was used to determine NPL thickness and were obtained on a Bruker Innova SPM instrument housed on a TMC vibration isolation table, utilizing tapping mode and silicon MikroMasch noncontact cantilever probes (HQ:NSC14). Samples were drop-cast onto freshly cleaved highly ordered pyrolitic graphite and vacuum dried.

Conflicts of interest

The authors declare no competing financial interests.

Acknowledgements

W.Z. acknowledges support from ACS Petroleum Research Fund (Award Number 59861-DNI5), NSF CAREER grant (Award Number CHE-1944978), NSF IUCRC Phase I grant (Award Number: 2052611), and Syracuse University under the Collaboration for Unprecedented Success and Excellence (CUSE) Grant (SD-10-2020). G. L. Gratefully acknowledges financial support from the USDA National Institute of Food and Agriculture, McIntire Stennis Program project Accession No. 1023017, NYZ1161219 project. We thank Farhana F. Syed and Hediyeh Zamani for assistance with EPR and AFM measurements, respectively.

References

1 J. Li, C. C. Stoumpos, G. G. Trimarchi, I. Chung, L. Mao, M. Chen, M. R. Wasielewski, L. Wang, M. G. Kanatzidis, *Chem. Mater.* **2018**, *30*, 4847-4856.
2 M. B. Faheem, B. Khan, C. Feng, M. U. Farooq, F. Raziq, Y. Xiao, Y. Li, *ACS Energy Lett.* **2019**, *5*, 290-320.
3 M. Kulbak, S. Gupta, N. Kedem, I. Levine, T. Bendikov, G. Hodes, D. Cahen, *J. Phys. Chem. Lett.* **2016**, *7*, 167-172.
4 J. Li, L. Xu, T. Wang, J. Song, J. Chen, J. Xue, Y. Dong, B. Cai, Q. Shan, B. Han, H. Zeng, *Adv. Mater.* **2017**, *29*, 1603885.
5 A. B. Wong, Y. Bekenstein, J. Kang, C. S. Kley, D. Kim, N. A. Gibson, D. Zhang, Y. Yu, S. R. Leone, L. W. Wang, A. P. Alivisatos, P. Yang, *Nano Lett.* **2018**, *18*, 2060-2066.
6 N. Kedem, T. M. Brenner, M. Kulbak, N. Schaefer, S. Levcenko, I. Levine, D. Abou-Ras, G. Hodes, D. Cahen, *J. Phys. Chem. Lett.* **2015**, *6*, 2469-2476.
7 R. Ketavath, N. K. Katturi, S. G. Ghugal, H. K. Kolli, T. Swetha, V. R. Soma, B. Murali, *J. Phys. Chem. Lett.* **2019**, *10*, 5577-5584.
8 H. Zhang, Z. H. Zhan, C. Ma, Y. Q. Liu, H. P. Xie, S. Q. Luo, Y. B. Yuan, Y. L. Gao, Y. Zhang, W. Q. Ming, Y. Liu, A. L. Pan, B. Yang, *J. Mater. Chem. C* **2019**, *7*, 5488-5496.
9 S. Bera, D. Ghosh, A. Dutta, S. Bhattacharyya, S. Chakraborty, N. Pradhan, *ACS Energy Lett.* **2019**, *4*, 1364-1369.
10 X. Zhang, H. Liu, W. Wang, J. Zhang, B. Xu, K. L. Karen, Y. Zheng, S. Liu, S. Chen, K. Wang, X. W. Sun, *Adv. Mater.* **2017**, *29*, 1606405.
11 X. Zhang, W. Wang, B. Xu, H. Liu, H. Shi, H. Dai, X. Zhang, S. Chen, K. Wang, X. W. Sun, *ACS Appl. Mater. Interfaces* **2018**, *10*, 24242-24248.
12 I. Lignos, V. Morad, Y. Shynkarenko, C. Bernasconi, R. M. Maceiczyk, L. Protesescu, F. Bertolotti, S. Kumar, S. T. Ochsenbein, N. Masciocchi, A. Guagliardi, C. J. Shih, M. I. Bodnarchuk, A. J. deMello, M. V. Kovalenko, *ACS Nano* **2018**, *12*, 5504-5517.
13 B. Xu, W. G. Wang, X. L. Zhang, W. Y. Cao, D. Wu, S. Liu, H. T. Dai, S. M. Chen, K. Wang, X. W. Sun, *J. Mater. Chem. C* **2017**, *5*, 6123-6128.
14 B. Wang, J. Iocozzia, M. Zhang, M. Ye, S. Yan, H. Jin, S. Wang, Z. Zou, Z. Lin, *Chem. Soc. Rev.* **2019**, *48*, 4854-4891.
15 Z.-J. Li, E. Hofman, A. H. Davis, M. M. Maye, W. Zheng, *Chem. Mater.* **2018**, *30*, 3854-3860.

16 Y. Guo, F. Zhao, Z. Li, J. Tao, D. Zheng, J. Jiang, J. Chu, *Org. Electron* **2020**, *83*, 105731.
17 D. Bai, J. Zhang, Z. Jin, H. Bian, K. Wang, H. Wang, L. Liang, Q. Wang, S. F. Liu, *ACS Energy Lett.* **2018**, *3*, 970-978.
18 U. Khan, Y. Zhinong, A. A. Khan, A. Zulfiqar, N. Ullah, *Nanoscale Res. Lett.* **2019**, *14*, 116.
19 A. M. Elseman, M. M. Rashad, A. M. Hassan, *ACS Sustain Chem. Eng.* **2016**, *4*, 4875-4886.
20 S. D. Stranks, H. J. Snaith, *Nat. Nanotechnol* **2015**, *10*, 391-402.
21 J. Shamsi, A. S. Urban, M. Imran, L. De Trizio, L. Manna, *Chem. Rev.* **2019**, *119*, 3296-3348.
22 M. H. Kumar, S. Dharani, W. L. Leong, P. P. Boix, R. R. Prabhakar, T. Baikie, C. Shi, H. Ding, R. Ramesh, M. Asta, M. Graetzel, S. G. Mhaisalkar, N. Mathews, *Adv. Mater.* **2014**, *26*, 7122-7127.
23 J. H. Im, I. H. Jang, N. Pellet, M. Gratzel, N. G. Park, *Nat. Nanotechnol.* **2014**, *9*, 927-932.
24 P. Tyagi, S. M. Arveson, W. A. Tisdale, *J. Phys. Chem. Lett.* **2015**, *6*, 1911-1916.
25 D. J. Yu, B. Cai, F. Cao, X. M. Li, X. H. Liu, Y. Zhu, J. P. Ji, Y. Gu, H. B. Zeng, *Adv. Mater. Interfaces* **2017**, *4*, 1700441.
26 S. Sun, D. Yuan, Y. Xu, A. Wang, Z. Deng, *ACS Nano* **2016**, *10*, 3648-3657.
27 B. Luo, Y. C. Pu, S. A. Lindley, Y. Yang, L. Lu, Y. Li, X. Li, J. Z. Zhang, *Angew. Chem. Int. Ed. Engl.* **2016**, *55*, 8864-8868.
28 S. Yun, A. Kirakosyan, S. G. Yoon, J. Choi, *ACS Sustain Chem. Eng.* **2018**, *6*, 3733-3738.
29 C. Liu, J. Lin, W. Zhai, Z. K. Wen, X. He, M. M. Yu, Y. Huang, Z. L. Guo, C. Yu, C. C. Tang, *RSC Adv.* **2019**, *9*, 39315-39322.
30 H. Huang, Y. Li, Y. Tong, E. P. Yao, M. W. Feil, A. F. Richter, M. Doblinger, A. L. Rogach, J. Feldmann, L. Polavarapu, *Angew. Chem. Int. Ed. Engl.* **2019**, *58*, 16558-16562.
31 Z. Dang, B. Dhanabalan, A. Castelli, R. Dhall, K. C. Bustillo, D. Marchelli, D. Spirito, U. Petralanda, J. Shamsi, L. Manna, R. Krahne, M. P. Arciniegas, *Nano Lett.* **2020**, *20*, 1808-1818.
32 H. Huang, Q. Xue, B. Chen, Y. Xiong, J. Schneider, C. Zhi, H. Zhong, A. L. Rogach, *Angew. Chem. Int. Ed. Engl.* **2017**, *56*, 9571-9576.
33 E. A. Tsiwah, Y. X. Ding, Z. X. Li, Z. Y. Zhao, M. Q. Wang, C. Hu, X. Q. Liu, C. H. Sun, X. J. Zhao, Y. Xie, *Crysteng. Comm.* **2017**, *19*, 7041-7049.
34 D. Zhang, S. W. Eaton, Y. Yu, L. Dou, P. Yang, *J. Am. Chem. Soc.* **2015**, *137*, 9230-9233.
35 Q. Pan, H. Hu, Y. Zou, M. Chen, L. Wu, D. Yang, X. Yuan, J. Fan, B. Sun, Q. Zhang, *J. Mater. Chem. C* **2017**, *5*, 10947-10954.
36 J. Shamsi, Z. Dang, P. Bianchini, C. Canale, F. D. Stasio, R. Brescia, M. Prato, L. Manna, *J. Am. Chem. Soc.* **2016**, *138*, 7240-7243.
37 Q. A. Akkerman, S. G. Motti, A. R. Srimath Kandada, E. Mosconi, V. D'Innocenzo, G. Bertoni, S. Marras, B. A. Kamino, L. Miranda, F. De Angelis, A. Petrozza, M. Prato, L. Manna, *J. Am. Chem. Soc.* **2016**, *138*, 1010-1016.
38 D. Chen, X. Chen, J. Li, X. Li, J. Zhong, *Dalton Trans.* **2018**, *47*, 9845-9849.
39 Y. Bekenstein, B. A. Koscher, S. W. Eaton, P. Yang, A. P. Alivisatos, *J. Am. Chem. Soc.* **2015**, *137*, 16008-16011.
40 A. H. Davis, W. Zheng, *J. Energy Chem.* **2021**, *59*, 257-275.
41 R. Qu, L. Zou, X. Qi, C. Liu, W. Zhao, J. Yan, Z. Zhang, Y. Wu, *CrystEngComm* **2020**, *22*, 1853-1857.
42 K.-H. Wang, L. Wu, L. Li, H.-B. Yao, H.-S. Qian, S.-H. Yu, *Angew. Chem. Int. Ed.* **2016**, *55*, 8328-8332.
43 S. Sun, D. Yuan, Y. Xu, A. Wang, Z. Deng, *ACS Nano* **2016**, *10*, 3648-3657.
44 S. Wei, Y. Yang, X. Kang, L. Wang, L. Huang, D. Pan, *Chem. Commun.* **2016**, *52*, 7265-7268.
45 H. Yang, Y. Zhang, J. Pan, J. Yin, O. M. Bakr, O. F. Mohammed, *Chem. Mater.* **2017**, *29*, 8978-8982.
46 L. Yang, D. Li, C. Wang, W. Yao, H. Wang, K. Huang, *J. Nanoparticle Res.* **2017**, *19*, 258.
47 J. A. Sichert, Y. Tong, N. Mutz, M. Vollmer, S. Fischer, K. Z. Milowska, R. Garcia Cortadella, B. Nickel, C. Cardenas-Daw, J. K. Stolarczyk, A. S. Urban, J. Feldmann, *Nano Lett.* **2015**, *15*, 6521-6527.
48 Z. Yuan, Y. Shu, Y. Tian, Y. Xin, B. Ma, *Chem. Commun.* **2015**, *51*, 16385-16388.
49 B. J. Bohn, Y. Tong, M. Gramlich, M. L. Lai, M. Doblinger, K. Wang, R. L. Z. Hoye, P. Muller-Buschbaum, S. D. Stranks, A. S. Urban, L. Polavarapu, J. Feldmann, *Nano Lett.* **2018**, *18*, 5231-5238.
50 G. Leem, S. Sarangi, S. Zhang, I. Rusakova, A. Brazdeikis, D. Litvinov, T. R. Lee, *Cryst. Growth Des.* **2009**, *9*, 32-34.
51 A. Pan, B. He, X. Fan, Z. Liu, J. J. Urban, A. P. Alivisatos, L. He, Y. Liu, *ACS Nano* **2016**, *10*, 7943-7954.
52 M. Kazes, T. Udayabhaskararao, S. Dey, D. Oron, *Acc. Chem. Res.* **2021**, *54*, 1409-1418.
53 J. Zhao, S. Cao, Z. Li, N. Ma, *Chem. Mater.* **2018**, *30*, 6737-6743.
54 F. Bertolotti, G. Nedelcu, A. Vivani, A. Cervellino, N. Masciocchi, A. Guagliardi, M. V. Kovalenko, *ACS Nano* **2019**, *13*, 14294-14307.
55 A. K. Guria, S. K. Dutta, S. Das Adhikari, N. Pradhan, *ACS Energy Lett.* **2017**, *2*, 1014-1021.
56 H. Liu, Z. Wu, J. Shao, D. Yao, H. Gao, Y. Liu, W. Yu, H. Zhang, B. Yang, *ACS Nano* **2017**, *11*, 2239-2247.
57 D. Parobek, B. J. Roman, Y. Dong, H. Jin, E. Lee, M. Sheldon, D. H. Son, *Nano Lett.* **2016**, *16*, 7376-7380.
58 S. Ithurria, P. Guyot-Sionnest, B. Mahler, B. Dubertret, *Phys. Rev. Lett.* **2007**, *99*, 265501.
59 Y. Yang, O. Chen, A. Angerhofer, Y. C. Cao, *J. Am. Chem. Soc.* **2006**, *128*, 12428-12429.
60 E. Hofman, R. J. Robinson, Z. J. Li, B. Dzikovski, W. Zheng, *J. Am. Chem. Soc* **2017**, *139*, 8878-8885.
61 Z. J. Li, E. Hofman, A. Blaker, A. H. Davis, B. Dzikovski, D. K. Ma, W. Zheng, *ACS Nano* **2017**, *11*, 12591-12600.
62 E. Hofman, A. Khammang, J. T. Wright, Z. J. Li, P. F. McLaughlin, A. H. Davis, J. M. Franck, A. Chakraborty, R. W. Meulenberg, W. Zheng, *J. Phys. Chem. Lett.* **2020**, *11*, 5992-5999.
63 N. Pradhan, *ChemPhysChem* **2016**, *17*, 1087-1094.
64 Z. J. Li, E. Hofman, A. H. Davis, A. Khammang, J. T. Wright, B. Dzikovski, R. W. Meulenberg, W. W. Zheng, *Chem. Mater.* **2018**, *30*, 6400-6409.
65 A. H. Davis, E. Hofman, K. Chen, Z. J. Li, A. Khammang, H. Zamani, J. M. Franck, M. M. Maye, R. W. Meulenberg, W. W. Zheng, *Chem. Mater.* **2019**, *31*, 2516-2523.
66 W. Zheng, Z. Wang, J. Wright, B. Goundie, N. S. Dalal, R. W. Meulenberg, G. F. Strouse, *J. Phys. Chem. C* **2011**, *115*, 23305-23314.
67 W. J. Mir, Y. Mahor, A. Lohar, M. Jagadeeswararao, S. Das, S. Mahamuni, A. Nag, *Chem. Mater* **2018**, *30*, 8170-8178.
68 Z. Li, M. Yang, J.-S. Park, S.-H. Wei, J. J. Berry, K. Zhu, *Chem. Mater.* **2015**, *28*, 284-292.